JGR Space Physics

RESEARCH ARTICLE
10.1029/2020JA029016

Key Points:

- Pc1 wave ducting is mainly observed over the SAA longitudes, possibly due to high Hall conductivity and plasma density there
- The seasonal distribution shows a higher occurrence during equinox and local summer than during local winter
- Both ionospheric plasma density and geomagnetic activity (or wave injection) contribute to the occurrence of ducting

Supporting Information:

- Supporting Information S1

Correspondence to:
H. Kim,
kim.hyangpyo@isee.nagoya-u.ac.jp

Citation:
Kim, H., Shiokawa, K., Park, J., Miyoshi, Y., Stolle, C., & Buchert, S. (2021). Statistical analysis of Pc1 wave ducting deduced from Swarm satellites. *Journal of Geophysical Research: Space Physics*, *126*, e2020JA029016. https://doi.org/10.1029/2020JA029016

Received 9 DEC 2020
Accepted 8 FEB 2021

Statistical Analysis of Pc1 Wave Ducting Deduced From Swarm Satellites

Hyangpyo Kim[1], Kazuo Shiokawa[1], Jaeheung Park[2,3], Yoshizumi Miyoshi[1], Claudia Stolle[4], and Stephan Buchert[5]

[1]Institute for Space-Earth Environmental Research, Nagoya University, Nagoya, Japan, [2]Korea Astronomy and Space Science Institute, Daejeon, South Korea, [3]Korea University of Science and Technology, Daejeon, South Korea, [4]GFZ German Research Centre for Geosciences, Potsdam, Germany, [5]Swedish Institute of Space Physics, Uppsala, Sweden

Abstract Transverse Pc1 waves propagating from magnetospheric source regions undergo mode conversion to the compressional mode in the ionosphere due to the induced Hall current. Mode converted Pc1 waves propagate across the magnetic field through the ionospheric waveguide. This process is called Pc1 wave ducting (PWD). PWDs have been observed by magnetometers on both ground and low Earth orbit satellites over a wide latitudinal and longitudinal range. In this work, we present the statistical analysis results of PWD exploiting Swarm satellites from 2015 to 2019. Spatial distributions show that the PWDs are mainly observed over the South Atlantic Anomaly longitudes, possibly due to the high Hall conductivity and F-region density, and at subauroral/auroral latitudes ($\pm 50^{\circ} - 70^{\circ}$ MLAT). The occurrence rate of PWD increases with increasing AE and |SYM-H| indices. Seasonal dependence shows that PWD exhibits a high occurrence rate during equinox and local summer while local winter hosts only a low occurrence. The asymmetry between summer and winter can be explained by the ionospheric plasma density. The high occurrence rate in equinox may result from intense geomagnetic activity during the equinox, probably due to the Russell-McPherron effect. From our statistical analysis, we conclude that the occurrence of PWD is controlled by both ionospheric plasma conditions and geomagnetic activity, and that the mode conversion and PWD occur more efficiently as plasma density increases.

1. Introduction

Pc1 waves are known as continuous geomagnetic pulsations observed in the ultralow frequency range (0.2–5 Hz). These waves are mainly generated in the inner magnetosphere by anisotropic distributions of energetic ions and often subsequent nonlinear processes, and are generally accepted as representing electromagnetic ion cyclotron (EMIC) wave (Anderson et al., 1996; Cornwall, 1965; Kennel & Petschek, 1966; Shoji et al., 2017). Pc1 waves initially propagate along the magnetic field as Alfvén mode with left-handed polarization. Then, they undergo mode conversion to right-handed or linear polarization during the propagation toward the Earth (e.g., Sakaguchi et al., 2013). Recently, Miyoshi et al. (2019) showed that EMIC waves are generated through the mode conversion from the equatorial noise at lower-L-shells. Once Pc1 waves reach the highly conductive ionosphere, the Alfvén mode Pc1 waves are converted to the compressional mode (or fast mode) by induced Hall currents. Afterward, they propagate across the magnetic field along the ionospheric waveguide within the F_2 layer. This process is called Pc1 wave ducting (PWD) (e.g., Fraser, 1975a, 1975b; Fujita & Tamao, 1988; Yoshikawa & Itonaga, 2000). Mode converted Pc1 wave can propagate over thousands of kilometers, even across the equator, and they are observed by magnetometers on both ground and low Earth orbit satellites (Kawamura et al., 1981; Kim, Hwang, Park, Miyashita, et al. (2018); Kim et al., 2010, 2011, 2020; Pisa et al., 2015).

Ducting Pc1 waves can be attenuated by absorption, scattering, and leakage, and the sustainability of PWD depends on the ionospheric conditions such as conductivity and plasma density, as well as the amplitude of the originally incident wave. From the observation by 13 induction magnetometers over the Canadian region, Hayashi et al. (1981) showed that Pc1 waves are attenuated with a rate of 10 dB/100 km (dB = decibel) in the injection center and of 2.5 dB/100 km beyond 500 km from the center. Kim et al. (2010), using an Antarctic magnetometer array, reported that the attenuation rate is between 8 and 20 dB/1,000 km. A follow-up statistical study conducted by Kim et al. (2011) showed that waveguide's cutoff frequency depends

on the ionospheric conductivity, that PWD on the ground is most efficient in the meridional direction, and that the wave attenuation increases with increasing frequency.

Using Swarm constellation and multiple ground-magnetometer chains, Kim, Hwang, Park, Miyashita, et al. (2018) reported the large-scale ducting of Pc1 waves both in the ionosphere and on the ground during a huge geomagnetic storm's recovery phase. They concluded that ionospheric waveguide could transmit Pc1 waves to a wide latitudinal and longitudinal range and that wave intensity abruptly decreases across sharp gradients in the ionospheric plasma density. A recent study by Kim et al. (2020) presented the relation between PWD and ionospheric plasma density inhomogeneities by exploiting the two adjoined Swarm satellites. They showed the changes of Pc1 wave intensity along the Swarm tracks generally follow the electron density variation and that the waves are stronger at higher-density regions. They also demonstrated that Pc1 waves are modulated and reflected when they cross plasma density irregularities such as equatorial plasma bubbles.

The studies mentioned above have shown ducting characteristics of Pc1 waves both on the ground and in the ionosphere. Still, the statistical characteristics of PWD within the ionosphere have not been reported. In this paper, we present the first-ever statistical analysis of the PWD within the ionosphere exploiting Swarm-A and Swarm-B data from 2015 to 2019. The morphology of ducted Pc1 waves is expected to be affected by ionospheric plasma density as well as the wave source regions in the magnetosphere. Hence, we investigated the spatial distribution of PWD, their dependence on geomagnetic activity (by comparing with the AE and SYM-H indices), the seasonal variation, and the relationship to plasma density.

2. Data and Analysis Procedure

2.1. Instruments

The Swarm constellation consists of three satellites placed in two different polar orbits within the ionospheric F layer. Swarm-A and Swarm-C fly side by side at an altitude of ~450 km, and Swarm-B moves alone at a higher altitude of ~510 km. Swarm is mainly designed to survey the geomagnetic field, and Vector Field Magnetometer onboard Swarm measures geomagnetic field vectors with a high sampling rate of 50 Hz, which can detect the electromagnetic waves in a frequency range up to 25 Hz. In order to analyze dependence on the plasma density, we used 2-Hz electron density data measured by the onboard Langmuir Probes. In this study, we used Swarm-A and Swarm-B because Swarm-C is very close to Swarm-A. The Altitude Adjusted Corrected Geomagnetic (AACGM) system (Shepherd, 2014) is used for transformation from geographic to geomagnetic coordinate.

2.2. Data Processing and Wave Detection Algorithm

We used a second-order Savitzky-Golay smoothing filter (Savitzky & Golay, 1964) to define the ambient magnetic field with a moving window of $\pm 15 \times 50$ data points (30 s). The fluctuating components can be obtained by subtracting the filtered from the measured magnetic field. We used local field-aligned coordinates to extract transverse (B_x: toward outer L-shells, B_y: toward magnetic east) and compressional (B_z: parallel to the ambient magnetic field) electromagnetic pulsations. A Fast Fourier Transform was performed with a window size of 2,048 data points (40.96 s), and then we obtained a complex Fourier signal ($F_{(x,y,z)}$) whose power is $\log(\left|\mathrm{F}_{(x,y,z)}\mathrm{nT}\right|^2)$ with 8,640 data blocks per day with 10-s time resolution.

In order to define PWD, we designed an automatic wave detection algorithm applied to the "compressional" magnetic pulsations (δB_z) as follows: Step 1. We subtracted the daily median values of wave power from the original wave power for each frequency. Step 2. Since diamagnetic effects caused by plasma irregularities can generate broadband pulsations of compressional magnetic field affecting the Pc1 frequency range (Ivarsen et al., 2019; Kim et al., 2020; Laundal et al., 2019; Lühr et al., 2014), we removed all signals at a specific time when the number of signals whose wave power exceeds 0.7 nT^2 at 0–0.46 Hz (20 frequency bins) is larger than 10. The frequencies at 0–0.46 Hz are inside typical frequency ranges plasma irregularities mainly affect. Step 3. Signals whose powers are <0.7 nT^2 and frequencies are outside the range of 0.2

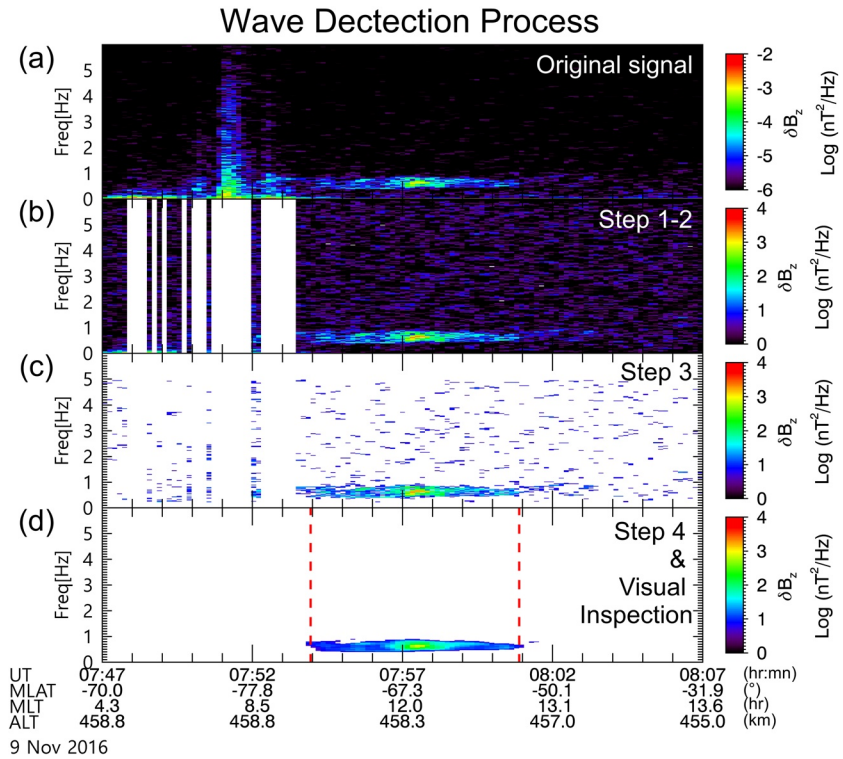

Figure 1. An example of wave detection process for the event on November 9, 2016 observed by Swarm-A. Dynamic spectrum of (a) original compressional wave, (b) compressional wave after taking Steps 1–2, and (c) compressional wave after taking Step 3. (d) Selected PWD event after taking Step 4 and visual inspection. PWD, Pc1 wave ducting.

and 5 Hz were removed. Step 4. A two-dimensional median filter (5 frequency steps × 5-time steps) was applied to eliminate the sharp stand-alone peaks. A compressional Pc1 wave packet, i.e., PWD, can be flagged when the signals satisfy both minimum bandwidth of 0.22 Hz (10 frequency bins) and minimum duration of 1 min. The events, however, for which wave power of a bottom frequency is not weaker than a factor of 1.5 of maximum wave power, are excluded because they may represent other types of pulsation or ambient noises (Erlandson & Anderson, 1996). Finally, we selected events through visual inspection by checking the well-structured narrowband spectral shape. Note that we only use the compressional components (δB_z) for the event detection, which distinguishes this study from previous ones. By only using the δB_z, we can focus on the PWD better than previous studies using either two perpendicular components (Park et al., 2013) or all the three components (Kim, Hwang, Park, Bortnik, et al., 2018). The latter approaches detect both ducted and nonducted (or directly injected) Pc1 waves, and are more vulnerable to magnetic disturbances by strong field-aligned currents at high latitudes.

Figure 1 shows an example of the wave detection process for an event on November 9, 2016 observed by Swarm-A. Figure 1a shows the dynamic spectrum of the original compressional wave, and Figures 1b and 1c present the spectrogram after taking Steps 1–2 and Step 3, respectively. In Figure 1d, we show a finally selected PWD event after taking Step 4 and visual inspection. This ducting event between 0.4 and 0.9 Hz starts from 07:54 UT and ends near 08:01 UT as marked by red dashed lines.

3. Statistical Results

Based on our wave detection algorithm, a total of 1,214 (1,128) PWD events are detected from Swarm-A (Swarm-B). In this section, we present the statistical dependence of detected PWDs on the location, geomagnetic indices, and seasons. Also, the relationship between PWD and ionospheric plasma density will be investigated. Note that we deduce statistical results by assigning each spectral data point to bins of 3°

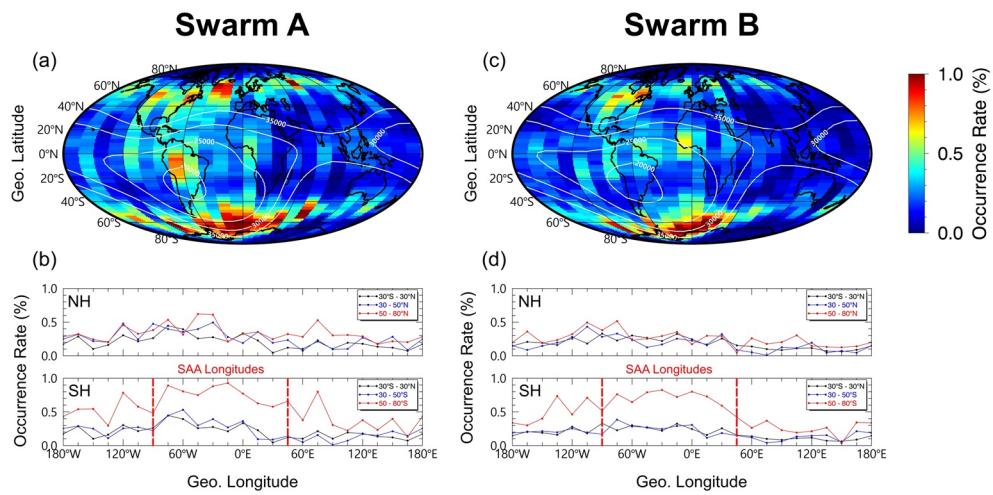

Figure 2. Geographic distribution of PWD observed by Swarm-A and Swarm-B with binning of 3° (latitude) and 15° (longitude). (a), (c) PWD occurrence rate. White lines indicate contours of averaged magnetic field strength measured by Swarm satellites. (b), (d) Averaged occurrence rate for five different magnetic latitude ranges (low: -30°-+30°, mid: ±30°-50°, and high: ±50°-80°S) of both hemispheres. The South Alantic Anomaly longitudes (90°W–45°E) are denoted by red dashed lines. PWD, Pc1 wave ducting.

(latitude) × 15° (longitude). The occurrence rate within each bin is estimated by dividing the number of data points for PWD events by those for total Swarm passes:

$$Occurrence\ rate\left(\%\right) = \frac{\sum Data\ points\ of\ PWD\ events}{\sum Data\ points\ of\ Swarm\ passes} \times 100$$

3.1. Spatial Distribution

Figure 2 shows the geographic distribution of the PWD occurrence rate observed by Swarm-A and Swarm-B. In the top two panels (Figures 2a and 2c), the colors indicate PWD occurrence rate, and white lines indicate the contours of averaged magnetic field strength measured by Swarm, indicating the South Atlantic Anomaly (SAA). The SAA is delimited from the East Pacific to South Africa with a magnetic field strength below 30,000 nT. Note that, in the present study, longitudes between 90°W and 45°E in the southern hemisphere are defined as "SAA longitudes," regardless of latitudes. The bottom panels (Figures 2b and 2d) represent the averaged occurrence rates for three different magnetic latitude (MLAT) ranges of both hemispheres (low: -30°-+30°, mid: ±30°-50°, and high: ±50°-80°) as a function of geographic longitude. Both satellite observations show that PWD can emerge at any ionospheric regions, and the overall occurrence is high at latitudes above 50° in both hemispheres. The interhemispheric asymmetry at subauroral and auroral latitudes clearly shows that the occurrence rate in the southern hemisphere (SH) is higher than in the northern hemisphere (NH). Elevated occurrence rates are shown around SAA longitudes at high latitudes as denoted by red dashed lines in Figures 2b and 2d. Also, considerable occurrence rates are manifest over low-latitude South America (or near the center of the SAA) for Swarm-A and over Western Africa for both satellites. The occurrence rate at Swarm-A is slightly higher than that of Swarm-B, but the overall distributions are similar between the two satellites. The Swarm tracks corresponding to PWD observation are plotted in Figure S1.

Figure 3 shows the occurrence distribution of PWD deduced from Swarm-A and Swarm-B as a function of magnetic local time (MLT) and MLAT on the SH and NH. We plot MLAT distribution between $\pm 20^{\circ} - 90^{\circ}$ since the AACGM do not provide accurate values below $\pm 20^{\circ}$ MLAT. PWDs are distributed over the whole MLTs in both hemispheres except around midnight, where occurrence rates are significantly low. Peak occurrences are clearly shown at 05–13 MLTs on SH from Swarm-B (Figure 3b). MLT dependence in the SH is clearer than in the NH at both satellite altitudes. For the MLAT dependence, the highest occurrence rate emerges around subauroral/auroral latitudes ($\pm 50^{\circ} - 70^{\circ}$ MLAT), which corresponds to the putative wave

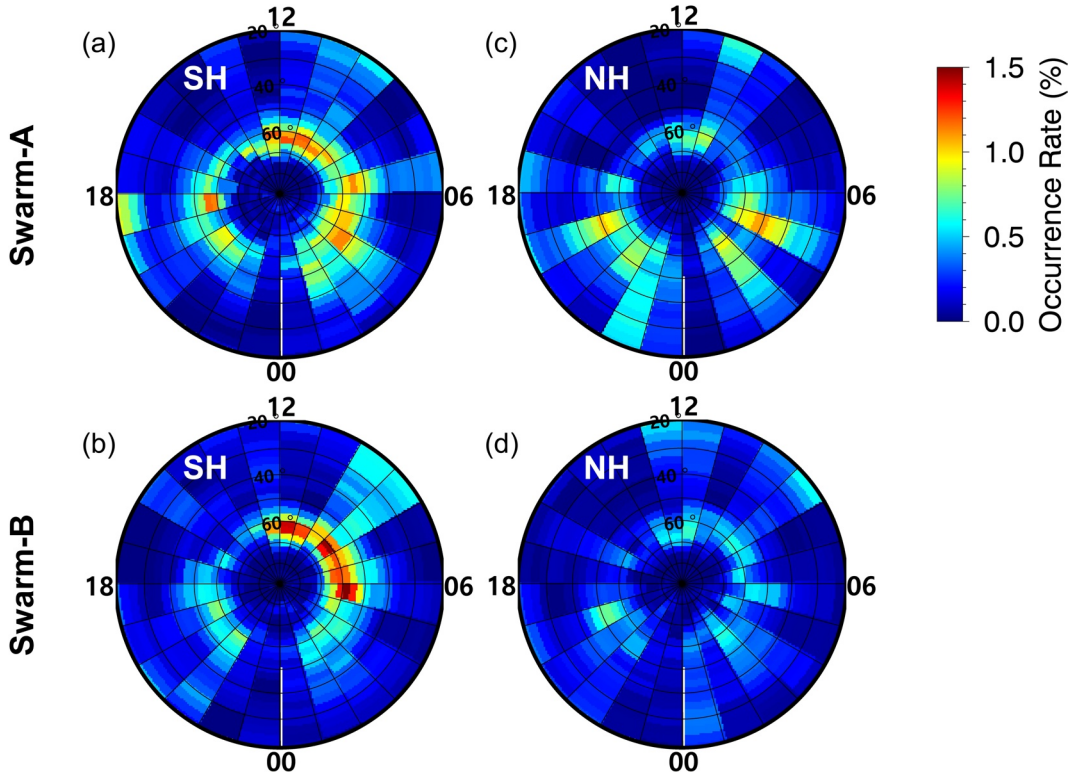

Figure 3. Geomagnetic distribution of PWD as a function of MLT and MLAT observed by (a), (c) Swarm-A in the SH and NH, respectively and (b), (d) Swarm-B. PWD, Pc1 wave ducting; MLT, magnetic local time; MLAT, magnetic latitude; SH, southern hemisphere; NH, northern hemisphere.

injection region L-shells (e.g., Wang et al., 2017, Table 1). Polar cap and cusp regions above ±70° MLAT show low occurrence rates.

3.2. Dependence on Geomagnetic Indices

Now we investigate the relation between PWD occurrence and geomagnetic activity. Pc1 wave occurrence in the ionosphere is not highly dependent on the Kp index (see Section 4.4 in Park et al., 2013 and Section 3.2 in Kim, Hwang, Park, Bortnik, et al., 2018), which is partly attributable to the low temporal resolution (3 h), logarithmic scales, and/or its representativeness for midlatitude geomagnetic observations (i.e., observations not directly under auroral or storm currents). Hence, we analyzed the geomagnetic dependence by comparing PWD activity with 1-min AE and SYM-H indices.

AE index is generally considered as a proxy for substorm activity. Note that we use AE dependence until February 28, 2018 since the index is unavailable after this time. Figure 4 shows the geographic distribution of PWD for three different ranges of AE index (AE < 100 nT, 100 < AE < 300 nT, and AE > 300 nT) deduced from Swarm-A. The top three panels indicate the number of data points for PWD events, and the middle panels present the occurrence rate. The bottomside panels show averaged occurrence rate for three different MLAT ranges of both hemispheres. The PWD occurrence at both high-latitude and low-latitude increases with increasing AE index, which implies that the Pc1 wave propagates well to low-latitude regions during the intense AE period. The occurrence rate deduced from Swarm-B also shows similar distributions, but slightly lower than that of Swarm-A (see Figure S2).

Next, we analyze the PWD occurrence dependence on the SYM-H index, which is often used as a measure of magnetic storm activity. Figure 5 shows the geographic distribution of PWD for three different ranges of SYM-H index (SYM-H > −10 nT, −20 < SYM-H < −10 nT, and SYM-H < − 20 nT) deduced from Swarm-A.

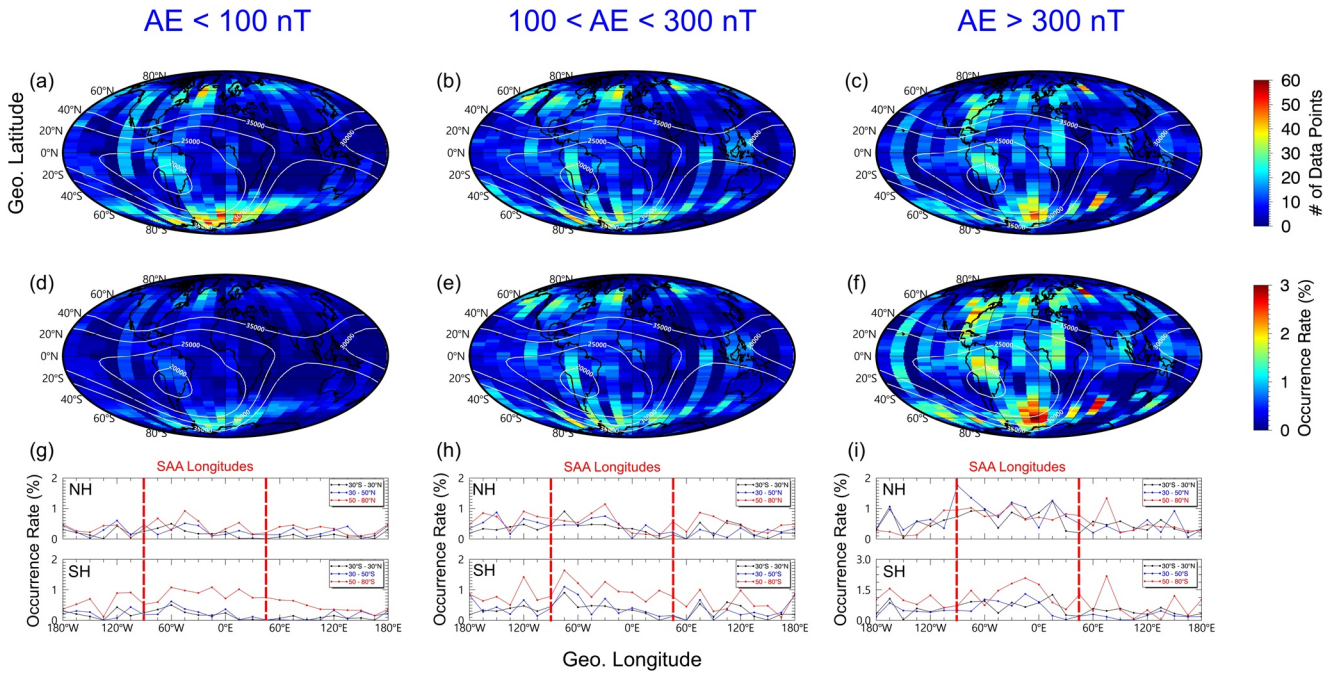

Figure 4. Geographic distribution of PWD occurrence for different ranges of AE index deduced from Swarm-A. (a–c) The number of data points for PWD events, (d–f) the occurrence rate of PWD, and (g–i) averaged occurrence rate for three different latitude ranges. PWD, Pc1 wave ducting.

Similarly to the AE dependence, it is also shown that the occurrence rate at both high-latitude and low-latitude increases with increasing |SYM-H| index. The occurrence rate deduced from Swarm-B shows similar distributions, but slightly lower than that of Swarm-A (see Figure S3).

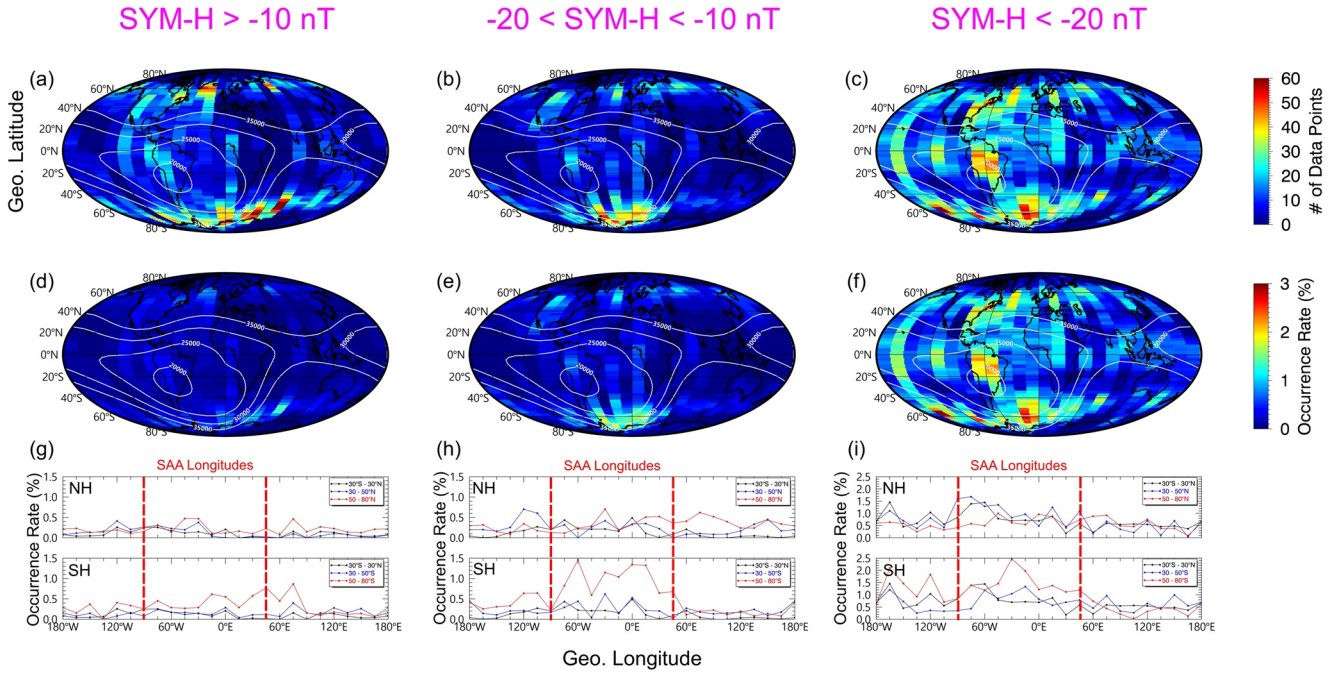

Figure 5. Geographic distribution of PWD occurrence for different ranges of SYM-H index deduced from Swarm-A. (a–c) The number of data points for PWD events, (d–f) the occurrence rate of PWD, and (g–i) averaged occurrence rate for three different latitude ranges. PWD, Pc1 wave ducting.

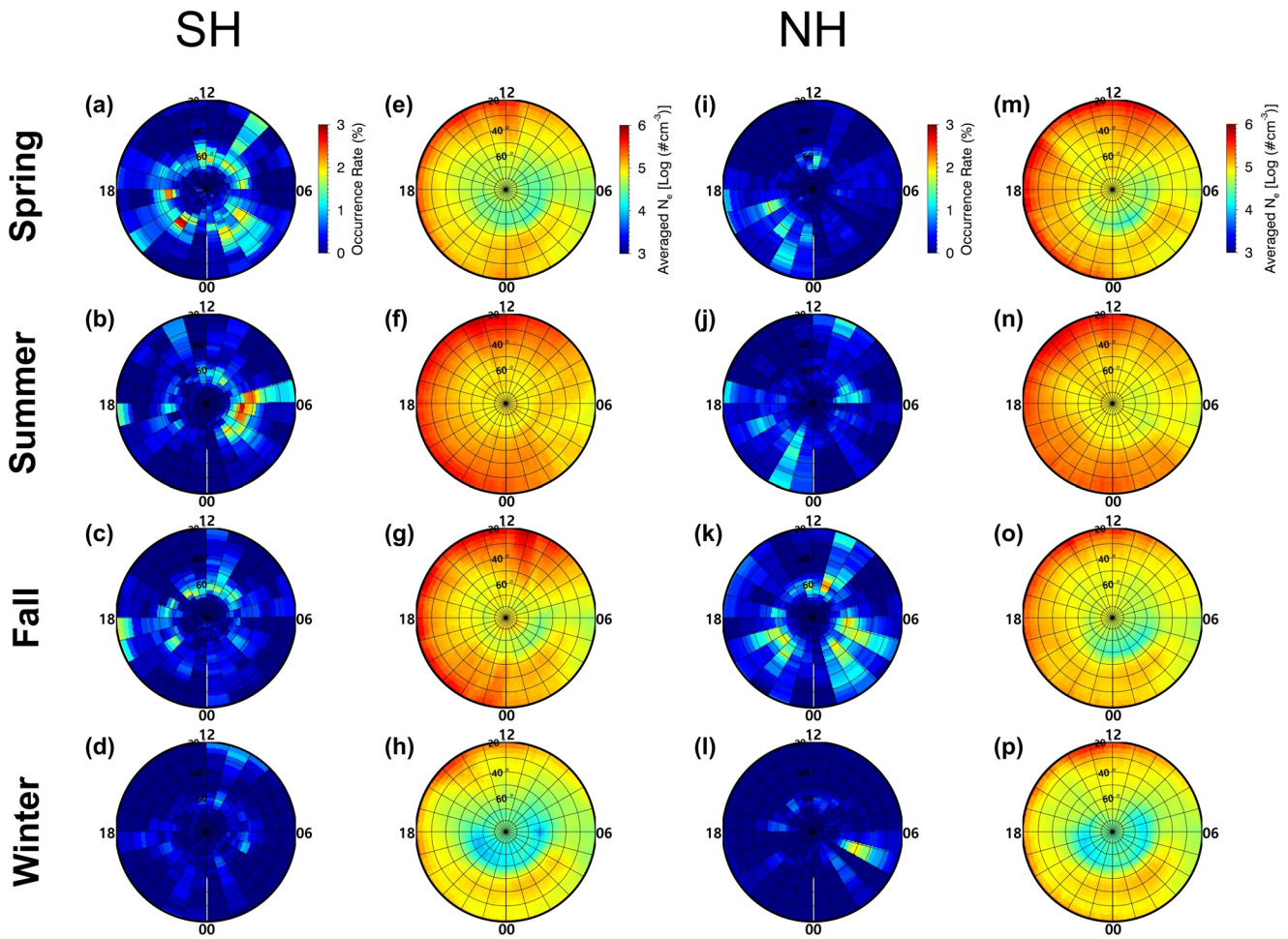

Figure 6. Seasonal distribution of (a–d and i–l) PWD occurrence rate and (e–h and m–p) averaged electron density (N_e) in the SH and NH as a function of MLT and MLAT observed by Swarm-A. PWD, Pc1 wave ducting. MLT, magnetic local time; MLAT, magnetic latitude; SH, southern hemisphere; NH, northern hemisphere.

3.3. Seasonal Dependence and Relationship With Plasma Density

In this section, we investigate seasonal variations of the PWD occurrence. Four seasons are defined, with the months hosting the equinox and solstice days as the center month. The seasons of the SH are classified as spring (August, September, and October), summer (November, December, and January), fall (February, March, and April), and winter (May, June, and July). The seasons of the NH are classified as spring (February, March, and April), summer (May, June, and July), fall (August, September, and October), and winter (November, December, and January). Since PWD is related to the ionospheric plasma density (Kim et al., 2020), which is controlled by the seasonal variation, we also compared PWD occurrence with electron density for each season.

Figure 6 shows the distribution of PWD occurrence and averaged electron density (N_e) for each season as a function of MLT and MLAT in both the SH and NH. The most remarkable feature is the lowest occurrence rate during the local winter in both hemispheres (Figures 6d and 6l). The N_e is also lowest during winter, especially around the putative wave injection region above $\pm 50^{\circ}$ MLAT (Figures 6h and 6p). For the other seasons, occurrence rates are high during spring and summer in the SH and during fall in the NH, but the difference among spring, summer, and fall seems mild. The N_e at midlatitude and high-latitude is highest during the local summer (Figures 6f and 6n), followed by equinox (Figures 6e, 6g, 6m, and 6o). The distribution of PWD occurrence and N_e deduced from Swarm-B also show the same features (see Figure S4).

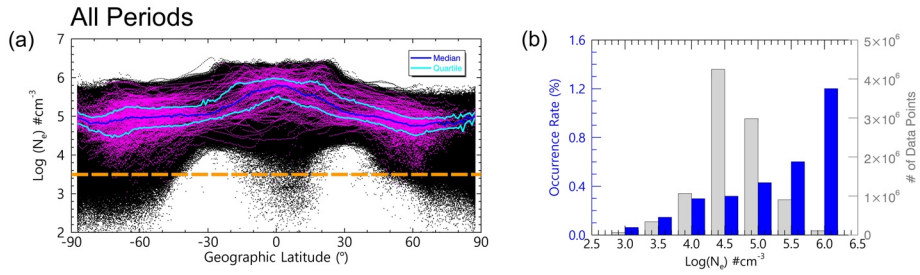

Figure 7. (a) Scatter plots of N_e deduced from Swarm-A for all Swarm passes. The black dots indicate N_e for each period, and the magenta dots indicate N_e when PWD is observed. Blue and cyan lines indicate the median and quartiles of N_e for magenta dots. (b) Occurrence rate of PWD for each N_e bin. The blue bar indicates occurrence rate, and the gray bar shows the number of data points for PWD events. PWD, Pc1 wave ducting.

Next, we plot N_e along Swarm orbits containing PWD events as a function of geographic latitude in Figure 7 (see Figure S5 for Swarm-B). We compare them with N_e of all the Swarm passes (i.e., those with and without PWD). In Figure 7a, the black dots indicate plasma density for all Swarm passes, and magenta dots represent plasma density when PWD is observed. Blue and cyan lines correspond to the median and quartiles of plasma density when Swarm encounters PWD. Pc1 wave seems to be mostly ducted when $N_e > \sim 10^{3.5}$ cm^{-3}, as marked by the dashed orange line. Figure 7b shows the occurrence rate as a function of ionospheric plasma density. We estimate it by dividing the number of data points for PWD events in Figure 7a by those for total Swarm passes at each of the 7 N_e intervals (7 bins in logscale). The occurrence rate (blue bars) shows that PWD mostly occurs when $N_e > \sim 10^{3.5}$ cm^{-3} and it increases with increasing N_e, which is consistent with the summer-winter asymmetry in Figure 6.

4. Discussion

4.1. Spatial Distribution

4.1.1. Longitude Dependence: Preference for the Regions Around the SAA

Our statistical results revealed that the peak occurrence of PWD in geographic coordinates appears around the SAA longitudes. The SAA is an area where Earth's inner radiation belt dips down to an altitude of ~200 km. This configuration leads to flux enhancement of energetic particles in this area, which increases conductivity at the bottomside of the ionosphere. According to Zossi et al. (2018), Hall conductivity is highest around the SAA longitudes. We interpret that the peak occurrence of PWD over the SAA longitudes is partly caused by the high Hall conductivity, which is favorable for mode conversion and ducting of Pc1 waves (Fujita & Tamao, 1988; Yoshikawa & Itonaga, 2000).

The high occurrence rate near the SAA longitudes in the SH can also be explained by F-region plasma density. In the nightside and morningside, the SH midlatitude F-region ionosphere around the SAA hosts high-density plasma during local summer (see Xiong & Lühr, 2014, Figure 2) and even in equinoxes (Jee et al., 2009, Figure 2). This phenomenon is known as the Weddell Sea Anomaly (WSA). Its location is not exactly at the center of the SAA, but still included in the SAA longitudes. The synergy between the SAA longitudes (weak magnetic field, high conductance, and efficient mode conversion) and the WSA (high-density F-region ducts) may explain the hotspot of "subauroral" PWD there.

The effect of the WSA on the subauroral PWD can be further confirmed by their local time dependences. According to Xiong and Lühr (2014, Figure 2), the peak of the WSA moves eastward from nightside to dayside via dawn. Figure S6 shows the PWD occurrence rate in the geographic map for both day (06–18 LT) and night (18-06 LT) times. The subauroral peaks of PWD occurrence move eastward from nightside to dayside, suggesting the connection between the PWD and the WSA.

Next, we discuss the "low-latitude" hotspots of PWD occurrence near the SAA longitudes. As seen in Figure S6, the low-latitude PWD events prefer daytime to nighttime. As plasma density in the low-latitude F-region is higher on the dayside than on the nightside (see also Figures 6e–6h and 6m–6p), this result implies that very high F-region density is necessary for Pc1 pulsations to penetrate from subauroral to low-latitude

regions. According to Xiong and Lühr (2014, Figure 1) and Jee et al. (2009, Figure 1), the effect of the WSA (both at night and in the morning) is not confined to subauroral regions, but extends toward the equator via South America. This may explain the low-latitude hotspots of PWD near South America.

However, we need to explain why the subauroral and low-latitude hotspots of PWD occurrence look interleaved with the midlatitude region of suppressed PWD occurrence (Figures 2a and 2c). If both hotspots represent Pc1 wave ducting from the subauroral toward the low-latitude ionosphere, they should be connected seamlessly instead of being separated by the midlatitude suppression. This discrepancy may be due to changes in wave normal angles (WNAs) during ionospheric ducting. For example, the Pc1 pulsations in Kim, Hwang, Park, Miyashita, et al. (2018, Figure 3b) exhibited WNA increases with decreasing latitudes, which eventually becomes ~90° at equatorial latitudes. In other words, the Pc1 pulsations were dominated by the compressional component at low latitudes, but transverse components became important or even dominant at midlatitudes. Our event detection method, which is based only on the compressional component, may overlook possible WNA changes during equatorward ducting.

The dominance of the compressional component at low latitudes may indicate that some waves are trapped in the equator due to equatorial ionospheric anomaly (EIA). According to Kim et al. (2020, Figures 2 and 3), PWD can be reflected and trapped by steep gradients in plasma density. The EIA may cause the enhancement of PWD occurrence at low latitudes.

4.1.2. Altitude Dependence

PWD occurrence rate deduced from Swarm-B is slightly lower than that of Swarm-A (see Figures 2 and 3). It may be because the Swarm-B altitude is farther from the main ducting layer (i.e., the F-region peak altitude around 350 km) than Swarm-A. This result implies that our statistics are not dominated by Pc1 waves coming directly from the magnetosphere down to the ionosphere (i.e., primary incident waves), but properly represent the secondary Pc1 waves that are mode converted below Swarm altitudes.

4.1.3. Local Time Dependence

According to magnetospheric observations close to the equatorial plane (i.e., the wave source region), EMIC waves are distributed across all MLTs with peak occurrence in dayside (dawn to dusk), and wave occurrence also depends on the source particle changes (Allen et al., 2016; Jun et al., 2019; Saikin et al., 2015; Usanova et al., 2012; Wang et al., 2017). Since PWD is more efficient in the meridional direction (Kim et al., 2011), the MLT distribution of PWD in the ionospheric altitudes should reflect the distribution in the wave source region. As we can see in Figure 3, our statistical results are consistent with previous studies in that PWD are distributed across all MLTs, and that clear peak occurrences are seen at dawn, noon, to dusk MLTs from both satellites (Figures 3a and 3b).

F-region plasma density seems to make an additional contribution to the MLT dependence of PWDs. In Figure 3, the MLT dependence appears clearer and better organized in the SH than in the NH: e.g., high occurrence rates in the early morning sector. According to Xiong and Lühr (2014, Figure 2), local time dependence of summer midlatitude ionospheric plasma is generally stronger in the SH than in the NH. Since PWD is positively affected by ionospheric density (e.g., Kim et al., 2020), PWD occurrence in the SH should show more conspicuous local time dependence than in the NH, which is actually seen in Figure 3.

4.1.4. Latitude Dependence

The highest occurrence at subauroral/auroral latitudes ($\pm 50^{\circ} - 70^{\circ}$ MLAT) seems because this region is close to the putative wave injection L-shells (e.g., Wang et al., 2017, Table 1), and because waves undergo attenuation and leakage during ionospheric ducting as it propagates away from the injection region (Kim et al., 2020). WNA changes, as mentioned in a preceding subsection, may further complicate the latitude dependence of compressional wave signatures in a nonmonotonic manner. Less PWDs in the polar cap and cusp ($> \pm 70°$ MLAT) may result from nearly ubiquitous ionospheric inhomogeneity there (e.g., Jin et al., 2020), interrupting poleward propagation of PWD. The high occurrence around the SAA contributes to the hemispheric asymmetry between the SH and the NH.

At low latitudes below $\pm 40^{\circ}$ MLAT, clear day-night asymmetry of PWD occurrence cannot be seen in our results, which is different from previous ground-based observations (e.g., Kawamura et al., 1981; Kuwashi-

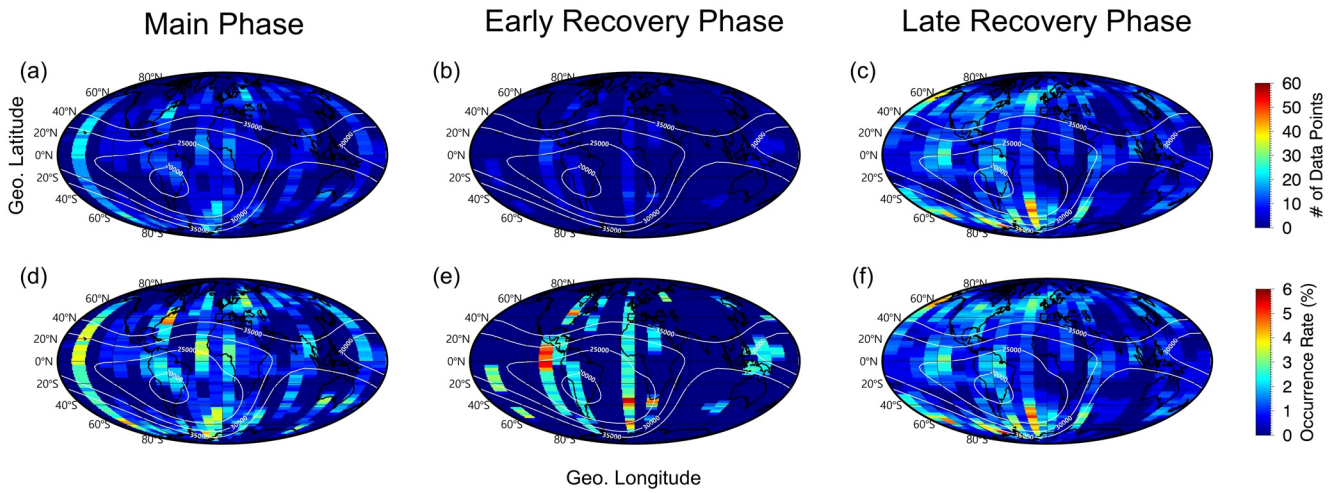

Figure 8. Geographic distribution of PWD occurrence for three geomagnetic storm phases deduced from Swarm-A. (a–c) The number of data points for PWD events (d–f) the occurrence rate of PWD. PWD, Pc1 wave ducting.

ma et al., 1981; Kwon et al., 2020). This is because a majority of Pc1 wave observed on the ground is mainly leaked signals from the ionospheric waveguide, i.e., the observation on the ground is highly affected by ionosphere-to-ground propagation condition. This may be why the MLT distribution is different between the ground and ionosphere. It is worth investigating Pc1 wave occurrence on the ground in relation to ionosphere-to-ground propagation conditions in future studies.

4.2. Dependence on Geomagnetic Activity

Our study shows the occurrence rate of PWD increases with increasing AE and |SYM-H| indices. According to Meredith et al. (2014) and Saikin et al. (2015), the spatial distributions of EMIC waves at source (i.e., equatorial) regions depend on the level of geomagnetic activity, and the occurrence rate increases with increasing AE index. Those behaviors agree with our results. A statistical study by Kim, Hwang, Park, Bortnik, et al. (2018) using Swarm satellites showed that 50% of the EMIC waves were found to be directly related to the geomagnetic storms, and that most of them occur during the late recovery phase (within 2–5 days following the storm main phase) with minimum occurrence during the early recovery phase.

In order to interpret our results in the same way as Kim, Hwang, Park, Bortnik, et al. (2018), we investigated the PWD occurrence rate for different phases of geomagnetic storms. We defined geomagnetic storms as periods with the minimum Dst index falling below −50 nT. A total of 63 storms were detected during the 5 years. We also categorized the storm intervals into the main phase, early recovery phase, and late recovery phase. The criteria for defining each storm phase are as follows: First, we pick up the minimum Dst value and then backtrack it until it reaches 0 nT. This interval is defined as the main phase. The endpoint of the early recovery phase is defined as the time when 50% of the minimum Dst is recovered. Finally, the endpoint of the late recovery phase is defined as the time of Dst, reaching 20% of the minimum.

Figure 8 shows the PWD occurrence distribution corresponding to each storm phase (see Figure S7 for Swarm-B). Most events are observed during the main and late recovery phase (Figures 8a and 8c), with the highest occurrence during the late recovery phase (Figure 8f). During the early recovery phase, though bins of high occurrence rates are observed here and there, the overall occurrence rate is still less than during other phases (Figure 8e).

One may argue that the azimuthal inhomogeneity, i.e., a high occurrence rate near the SAA longitudes, is related to the Swarm traveling along specific longitudes during strong geomagnetic activities. However, the occurrence rate near the SAA longitudes is elevated compared to other longitudes also during quiet time, as seen in Figures 4d, S2d, and S3d. This implies that the azimuthal inhomogeneity of Pc1 occurrence is not primarily affected by sampling bias combined with geomagnetic activities.

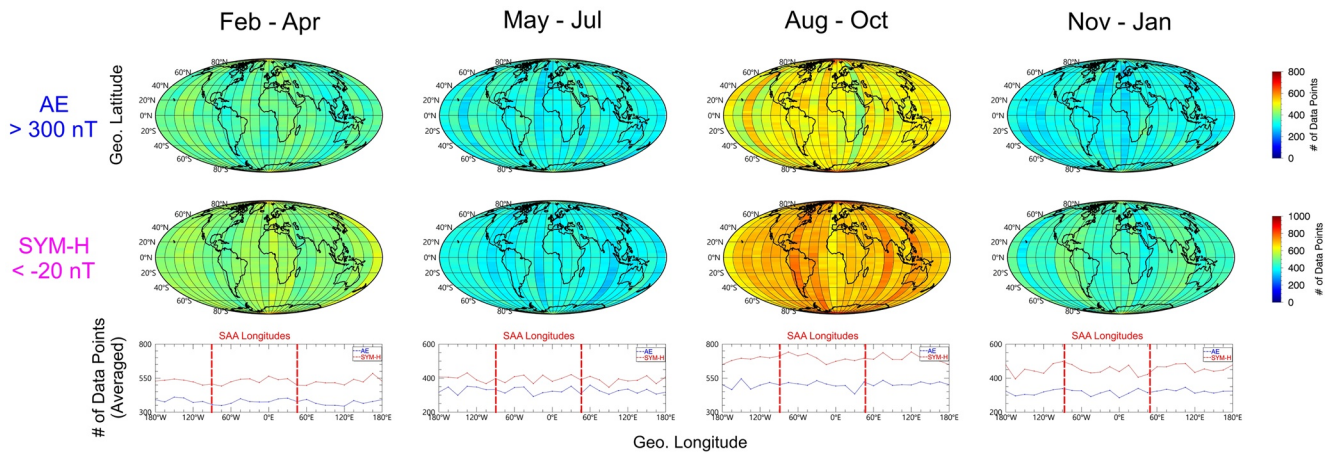

Figure 9. The number of Swarm-A data points for the strong geomagnetic activity (AE >300 nT and SYM-H <- 20 nT during 5 years (AE is between 2015 and February 2018). Bottom panels are averaged occurrence rate over all latitudes.

4.3. Seasonal Dependence and Relationship With Plasma Density

Now we discuss the seasonal dependence of PWD occurrence and compare them with plasma density climatology at Swarm altitudes. First, we focus on the plasma density (Figures 6e–6h and 6m–6p). Averaged plasma density generally conforms to the Chapman ionization theory in that density is higher during the local summer than winter: high solar zenith angle during summer is favorable to photoionize neutrals. The midlatitude trough leading to winter density decrease (e.g., Hong et al., 2019) also contributes to the low density in the winter hemisphere.

Next, we move to the PWD occurrence rate (Figures 6a–6d and 6i–6l). According to Kim et al. (2020), the intensity of PWD generally follows the ionospheric plasma density, i.e., the waves are stronger at regions with higher plasma density. This means that high-density regions are favorable for ionospheric ducting, and we expect that the occurrence rate is highest during summer. Occurrence rate asymmetry between the summer and winter hemispheres results from the different plasma densities as we expected. However, the occurrence during equinox is also as high as during the local summer, even highest during fall in the NH. The high occurrence rates in equinox may result from intense geomagnetic activity during the equinox, possibly due to the Russell-McPherron effect (Russell & McPherron, 1976). As we mentioned in previous sections, PWD is more frequently observed during geomagnetically active periods. Figure 9 shows the number of Swarm-A data points when strong geomagnetic activity (AE > 300 nT and SYM-H < −20 nT) took place during 5 years (AE is between 2015 and February 2018). As we can see, the duration (number of data points) of strong geomagnetic activity is longest during equinoxes, especially during August to October. This result can also explain why the hemispheric asymmetry of occurrence rate gradually weakens as AE and |SYM-H| indices increase (Figures 4 and 5).

In Figure 7, we compared plasma density for all Swarm passes with those during PWD detection. Direct comparisons between the plasma density and probability of PWD are difficult, because in our wave detection algorithm, we defined PWD only when the wave amplitude just satisfies > 0.7 nT^2 and did not analyze the wave amplitude itself. Still, Figure 7 firmly demonstrates that mode conversion and ducting of Pc1 waves occur more efficiently as N_e increases. However, one may argue that the high occurrence of PWD for a high-density background ionosphere is just a pure coincidence because both EMIC wave occurrence at the magnetospheric source regions (or geomagnetic activity) and plasma density are high for, e.g., high solar activity: that is, the ionospheric density and PWD occurrence may not be directly related. To address this issue, we repeat Figure 7 in Figure 10, but only for quiet periods (AE < 100 nT) (see Figure S8 for Swarm-B). As we can see in Figure 10a, most PWDs are distributed above $N_e > \sim 10^{3.5}$ cm^{-3} even during quiet times, and the quartiles are similar to those in Figure 7a. The occurrence rate in Figure 10b also shows similar positive trends to those seen in Figure 7b.

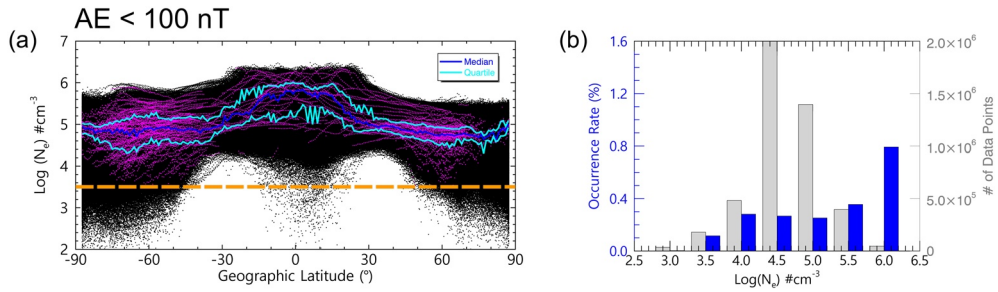

Figure 10. (a) Scatter plots of N_e and (b) PWD occurrence rate deduced from Swarm-A during a period of AE < 100 nT in the same format as that of Figure 7. PWD, Pc1 wave ducting.

The contribution of plasma density to the PWD occurrence rate is also supported by ionospheric plasma density variation during geomagnetic storms. According to Kumar and Parkinson (2017, Figure 4), ionospheric F-region density above $\pm 40^{\circ}$ MLAT, where Swarm usually encounters ducting events, generally decreases after geomagnetic storms, and the decrease is deeper during the early recovery phase than during the late recovery phase. This strong density decrease during the early recovery phase may contribute to the lowest occurrence rate of PWD during the early recovery phase of geomagnetic storms (Figure 8e).

Amplitudes of incident waves naturally play a key role in the wave ducting statistics in this study. That is, stronger incident waves have more chances to be detected by Swarm, even after long-distance ducting with significant attenuation. In addition to this effect, Figure 10 also suggests that a dense ionosphere also generates favorable conditions for Pc1 wave ducting. In short, the ducting statistics in this study seem to reflect the convolution of wave injection intensity (i.e., magnetospheric effects represented by geomagnetic indices) with ducting efficiency (i.e., ionospheric effects characterized by background density levels). However, further quantitative studies comparing the EMIC wave generation in the magnetosphere with PWD in the ionosphere are warranted, especially those based on the coordinated observations from multiple locations.

5. Summary

Based on the Swarm satellite data during 5 years, we analyzed spatial distributions of PWD and their dependence on the geomagnetic activity, seasons, and ionospheric plasma density. The main results obtained in this study are summarized as follows:

1. PWD has a hot spot over the South Atlantic Anomaly longitudes, possibly due to high Hall conductivity and F-region density there
2. The occurrence rate of PWD is highest around subauroral/auroral latitudes ($\pm 50^{\circ} - 70^{\circ}$ MLAT), which are generally known to be wave injection regions, and those in the southern hemisphere are higher than in the northern hemisphere
3. PWD exhibits high occurrence rates during equinoxes and local summer, while local winter hosts only a low occurrence rate. The asymmetry between the summer and winter can be attributed to the ionospheric plasma density, and the high occurrence rate during equinoxes may result from strong geomagnetic activity in those seasons
4. The occurrence rate of PWD increases with increasing values of both AE and |SYM-H| indices
5. Both high ionospheric plasma density and high geomagnetic activity contribute to the occurrence of PWD. The former and the latter may be interpreted as ducting efficiency and incident wave activity, respectively
6. PWD mostly occurs when $N_e > \sim 10^{3.5}$ cm^{-3}, and mode conversion and ducting occur more efficiently as N_e increases

Data Availability Statement

The Swarm vector magnetic field and electron density data were obtained online from (http://swarm-diss.eo.esa.int). The AE and SYM-H indices data were downloaded online from OMNI web database (https://omniweb.gsfc.nasa.gov).

Acknowledgments
The authors thank the ESA and Swarm team for providing the data to the public. This work was supported by the JSPS KAKENHI (15H05815, 15H05747, 16H06286, 17H00728, and 20H01959).

References

Allen, R. C., Zhang, J.-C., Kistler, L. M., Spence, H. E., Lin, R.-L., Klecker, B., et al. (2016). A statistical study of EMIC waves observed by cluster: 2. Associated plasma conditions. *Journal of Geophysical Research: Space Physics*, *121*, 6458–6479. https://doi.org/10.1002/2016JA022541

Anderson, B. J., Denton, R. E., Ho, G., Hamilton, D. C., Fuselier, S. A., & Strangeway, R. J. (1996). Observational test of local proton cyclotron instability in the Earth's magnetosphere. *Journal of Geophysical Research*, *101*(A10), 21527–21543. https://doi.org/10.1029/96JA01251

Cornwall, J. M. (1965). Cyclotron instabilities and electromagnetic emission in the ultralow frequency and very low frequency ranges. *Journal of Geophysical Research*, *70*(1), 61–69. https://doi.org/10.1029/JZ070i001p00061

Erlandson, R. E., & Anderson, B. J. (1996). Pc 1 waves in the ionosphere: A statistical study. *Journal of Geophysical Research*, *101*(A4), 7843–7857. https://doi.org/10.1029/96JA00082

Fedorov, E. N., Pilipenko, V. A., Engebretson, M. J., & Hartinger, M. D. (2018). Transmission of a magnetospheric Pc1 wave beam through the ionosphere to the ground. *Journal of Geophysical Research: Space Physics*, *123*, 3965–3982. https://doi.org/10.1029/2018JA025338

Fraser, B. J. (1975a). Polarization of Pc 1 pulsations at high and middle latitudes. *Journal of Geophysical Research*, *80*(19), 2797–2807. https://doi.org/10.1029/ja080i019p02797

Fraser, B. J. (1975b). Ionospheric duct propagation and Pc 1 pulsation sources. *Journal of Geophysical Research*, *80*(19), 2790–2796. https://doi.org/10.1029/ja080i019p02790

Fujita, S., & Tamao, T. (1988). Duct propagation of hydromagnetic waves in the upper ionosphere. 1. Electromagnetic field distributions in high latitudes associated with localized incidence of a shear Alfvén wave. *Journal of Geophysical Research*, *93*(A12), 14665–14673. https://doi.org/10.1029/JA093iA12p14665

Hayashi, K., Kokubun, S., Oguti, T., Tsuruda, K., Machida, S., Kitamura, T., et al. (1981). The extent of Pc 1 source region in high latitudes. *Canadian Journal of Physics*, *59*, 1097–1105.

Hong, J., Kim, Y. H., & Lee, Y.-S. (2019). Characteristics of the ionospheric mid-latitude trough measured by topside sounders in 1960-70s. *Journal of Astronomy and Space Sciences*, *36*(3), 121–131. https://doi.org/10.5140/JASS.2019.36.3.121

Ivarsen, M. F., Jin, Y., Spicher, A., & Clausen, L. B. N. (2019). Direct evidence for the dissipation of small-scale ionospheric plasma structures by a conductive E region. *Journal of Geophysical Research: Space Physics*, *124*, 2935–2942. https://doi.org/10.1029/2019JA026500

Jee, G., Burns, A. G., Kim, Y. -H., & Wang, W. (2009). Seasonal and solar activity variations of the Weddell Sea Anomaly observed in the TOPEX total electron content measurements. *Journal of Geophysical Research*, *114*, A04307. https://doi.org/10.1029/2008JA013801

Jin, Y., Xiong, C., Clausen, L., Spicher, A., Kotova, D., Brask, S., et al. (2020). Ionospheric plasma irregularities based on in situ measurements from the Swarm satellites. *Journal of Geophysical Research: Space Physics*, *124*, e2020JA028103. https://doi.org/10.1029/2020JA028103

Jun, C. W., Yue, C., Bortnik, J., Lyons, L. R., Nishimura, Y., Kletzing, C., et al. (2019). A statistical study of EMIC waves associated with and without energetic particle injection from the magnetotail. *Journal of Geophysical Research: Space Physics*, *124*, 433–450. https://doi.org/10.1029/2018JA025886

Kawamura, M., Kuwashima, M., & Toya, T. (1981). Comparative study of magnetic Pc1 pulsations between low latitudes and high latitudes: Source region and propagation mechanism of the waves deduced from the characteristics of the pulsations at middle and low latitudes. *Memoirs of National Institute of Polar Research*, *18*, 83–100.

Kennel, C. F., & Petschek, H. E. (1966). Limit on stably trapped particle fluxes. *Journal of Geophysical Research*, *71*(1), 1–28. https://doi.org/10.1029/JZ071i001p00001

Kim, H., Hwang, J., Park, J., Bortnik, J., & Lee, J. (2018). Global characteristics of electromagnetic ion cyclotron waves deduced from Swarm satellites. *Journal of Geophysical Research: Space Physics*, *123*, 1325–1336. https://doi.org/10.1002/2017JA024888

Kim, H., Hwang, J., Park, J., Miyashita, Y., Shiokawa, K., Mann, I. R., et al. (2018). Large-scale ducting of Pc1 pulsations observed by Swarm satellites and multiple ground networks. *Geophysical Research Letters*, *45*, 12703–12712. https://doi.org/10.1029/2018GL080693

Kim, H., Lessard, M. R., Engebretson, M. J., & Lühr, H. (2010). Ducting characteristics of Pc 1 waves at high latitudes on the ground and in space. *Journal of Geophysical Research*, *115*, A09310. https://doi.org/10.1029/2010JA015323

Kim, H., Lessard, M. R., Engebretson, M. J., & Young, M. A. (2011). Statistical study of Pc1–2 wave propagation characteristics in the high-latitude ionospheric waveguide. *Journal of Geophysical Research*, *116*, A07227. https://doi.org/10.1029/2010JA016355

Kim, H., Shiokawa, K., Park, J., Miyoshi, Y., Hwang, J., & Kadokura, A. (2020). Modulation of Pc1 wave ducting by equatorial plasma bubble. *Geophysical Research Letters*, *47*, e2020GL088054. https://doi.org/10.1029/2020GL088054

Kumar, V. V., & Parkinson, M. L. (2017). A global scale picture of ionospheric peak electron density changes during geomagnetic storms. *Space Weather*, *15*, 637–652. https://doi.org/10.1002/2016SW001573

Kuwashima, M., Toya, T., Kawamura, M., Hirasawa, T., Fukunishi, H., & Ayukawa, M. (1981). Comparative study of magnetic Pc1 pulsations between low latitudes and high latitudes: Statistical study. *Memoirs of National Institute of Polar Research-Special Issue*, *18*, 101–117.

Kwon, J. W., Kim, K. H., Jin, H., Kwon, H. J., Jee, G., Shiokawa, K., & Connors, M. (2020). Statistical study of EMIC Pc1-Pc2 waves observed at subauroral latitudes. *Journal of Atmospheric and Solar-Terrestrial Physics*, *205*, 105292. https://doi.org/10.1016/j.jastp.2020.105292

Laundal, K. M., Hatch, S. M., & Moretto, T. (2019). Magnetic effects of plasma pressure gradients in the upper F region. *Geophysical Research Letters*, *46*, 2355–2363. https://doi.org/10.1029/2019GL081980

Lühr, H., Park, J., Xiong, C., & Rauberg, J. (2014). Alfvén wave characteristics of equatorial plasma irregularities in the ionosphere derived from CHAMP observations. *Frontiers in Physics*, *2*, 47. https://doi.org/10.3389/fphy.2014.00047

Meredith, N. P., Horne, R. B., Kersten, T., Fraser, B. J., & Grew, R. S. (2014). Global morphology and spectral properties of EMIC waves derived from CRRES observations. *Journal of Geophysical Research: Space Physics*, *119*, 5328–5342. https://doi.org/10.1002/2014JA020064

Miyoshi, Y., Matsuda, S., Kurita, S., Nomura, K., Keika, K., Shoji, M., et al. (2019). EMIC waves converted from equatorial noise due to M/Q=2 ions in the plasmapshere: Observations from Van Allen Probes and Arase. *Geophysical Research Letters*, *46*, 5662–5669. https://doi.org/10.1029/2019GL083024

Park, J., Lühr, H., & Rauberg, J. (2013). Global characteristics of Pc1 magnetic pulsations during solar cycle 23 deduced from CHAMP data. *Annales Geophysicae*, *31*(9), 1507–1520. https://doi.org/10.5194/angeo-31-1507-2013

Pisa, D., Parrot, M., Santolík, O., & Menietti, J. D. (2015). EMIC waves observed by the low-altitude satellite DEMETER during the November 2004 magnetic storm. *Journal of Geophysical Research: Space Physics*, *120*, 5455–5464. https://doi.org/10.1002/2014JA020233

Russell, C. T., & McPherron, R. L. (1976). Semiannual variation of geomagnetic activity. *Journal of Geophysical Research*, *78*(1), 92–108. https://doi.org/10.1029/JA078i001p00092

Saikin, A. A., Zhang, J.-C., Allen, R. C., Smith, C. W., Kistler, L. M., Spence, H. E., et al. (2015). The occurrence and wave properties of H-, He-, and O-band EMIC waves observed by the Van Allen Probes. *Journal of Geophysical Research: Space Physics*, *120*, 7477–7492. https://doi.org/10.1002/2015JA021358

Sakaguchi, K., Kasahara, Y., Shoji, M., Omura, Y., Miyoshi, Y., Nagatsuma, T., et al. (2013). Akebono observations of EMIC waves in the slot region of the radiation belts. *Geophysical Research Letters*, *40*, 5587–5591. https://doi.org/10.1002/2013GL058258

Savitzky, A., & Golay, M. J. E. (1964). Smoothing and differentiation of data by simplified least squares procedures. *Analytical Chemistry*, *36*(8), 1627–1639. https://doi.org/10.1021/ac60214a047

Shepherd, S. G. (2014). Altitude-adjusted corrected geomagnetic coordinates: Definition and functional approximations. *Journal of Geophysical Research: Space Physics*, *119*, 7501–7521. https://doi.org/10.1002/2014JA020264

Shoji, M., Miyoshi, Y., Katoh, Y., Keika, K., Angelopoulos, V., Kasahara, S., et al. (2017). Ion hole formation and nonlinear generation of electromagnetic ion cyclotron waves: THEMIS observations. *Geophysical Research Letters*, *44*, 8730–8738. https://doi.org/10.1023/2017GL074254

Usanova, M. E., Mann, I. R., Bortnik, J., Shao, L., & Angelopoulos, V. (2012). THEMIS observations of electromagnetic ion cyclotron wave occurrence: Dependence on AE, SYMH, and solar wind dynamic pressure. *Journal of Geophysical Research*, *117*, A10218. https://doi.org/10.1029/2012JA018049

Wang, X. Y., Huang, S. Y., Allen, R. C., Fu, H. S., Deng, X. H., Zhou, M., et al. (2017). The occurrence and wave properties of EMIC waves observed by the Magnetospheric Multiscale (MMS) mission. *Journal of Geophysical Research: Space Physics*, *122*, 8228–8240. https://doi.org/10.1002/2017JA024237

Xiong, C., & Lühr, H. (2014). The midlatitude summer night anomaly as observed by CHAMP and GRACE: Interpreted as tidal features. *Journal of Geophysical Research: Space Physics*, *119*, 4905–4915. https://doi.org/10.1002/2014JA019959

Yoshikawa, A., & Itonaga, M. (2000). The nature of reflection and mode conversion of MHD waves in the inductive ionosphere: Multistep ode conversion between divergent and rotational electric fields. *Journal of Geophysical Research*, *105*(A5), 10565–10584. https://doi.org/10.1029/1999JA000159

Zossi, B. S., Elias, A. G., & Fagre, M. (2018). Ionospheric conductance spatial distribution during geomagnetic field reversals. *Journal of Geophysical Research: Space Physics*, *123*, 2379–2397. https://doi.org/10.1002/2017JA024925